nature photonics

LETTERS

PUBLISHED ONLINE: 20 MAY 2012 | DOI: 10.1038/NPHOTON.2012.109

Chemically etched ultrahigh-Q wedge-resonator on a silicon chip

Hansuek Lee†, Tong Chen†, Jiang Li†, Ki Youl Yang, Seokmin Jeon, Oskar Painter and Kerry J. Vahala*

Ultrahigh-Q optical resonators are being studied across a wide range of fields, including quantum information, nonlinear optics, cavity optomechanics and telecommunications[1–7]. Here, we demonstrate a new resonator with a record Q-factor of 875 million for on-chip devices. The fabrication of our device avoids the requirement for a specialized processing step, which in microtoroid resonators[8] has made it difficult to control their size and achieve millimetre- and centimetre-scale diameters. Attaining these sizes is important in applications such as microcombs and potentially also in rotation sensing. As an application of size control, stimulated Brillouin lasers incorporating our device are demonstrated. The resonators not only set a new benchmark for the Q-factor on a chip, but also provide, for the first time, full compatibility of this important device class with conventional semiconductor processing. This feature will greatly expand the range of possible 'system on a chip' functions enabled by ultrahigh-Q devices.

Achieving a long photon storage time (high Q-factor) in microcavities relies critically on the use of low-absorption dielectrics and the creation of very smooth (low-scattering) dielectric interfaces. Although crystalline resonators currently provide the highest Q-factors[9–11], in chip-compatible devices silica has by far the lowest intrinsic material loss. Microtoroid resonators combine this low material loss with a reflow technique in which surface tension is used to smooth lithographic and etch-related blemishes[8]. However, reflow smoothing makes it very challenging to fabricate larger-diameter ultrahigh-Q (UHQ) resonators or to leverage the full range of integration tools and devices available on silicon. The devices reported here attain UHQ performance using only conventional semiconductor processing methods on a silicon wafer. Moreover, the best Q performance occurs for diameters greater than 500 μm, a size range that is difficult to access with microtoroids because of the limitations of the reflow process. Microcombs will benefit from a combination of UHQ and larger-diameter resonators (microwave-rate free spectral range, FSR) to create combs that are efficient in turn-on power and can be self-referenced[6]. Two further applications that can benefit from larger (1–50 mm diameter) UHQ resonators are integrated reference cavities and ring gyroscopes.

We also demonstrate excellent control of the FSR, opening the possibility of precision repetition rate control in microcombs or precision control of the FSR. The latter is important in stimulated Brillouin lasers (SBLs), which have been demonstrated recently in UHQ silica microspheres, in calcium fluoride resonators[12,13] and in rib-waveguide Fabry–Perot resonators[14]. As an application of this control, SBLs are demonstrated here using these new resonators. The devices feature very low threshold turn-on power, milliwatt-scale output power and very high coherence.

Earlier work investigated the Q-factor in a wedge-shaped resonator fabricated from silica on a silicon wafer, and Q-factors as high as 50 million were obtained[15]. That approach isolated the mode from the lithographic blemishes near the outer rim of the resonator by using a shallow wedge angle. In the current work, we boost the optical Q by a factor of ∼20 beyond these earlier results through a combination of process improvements. Although the present devices resemble the earlier geometry[15], they derive their UHQ performance from changes to the etch process and oxide growth and not from the physical principle at work in the earlier structures, namely a shallow wedge angle to provide roughness isolation. Indeed, and in contrast to that earlier work, larger wedge angles are now desirable.

A top-view optical micrograph is provided in Fig. 1 to illustrate the basic geometry. The process flow begins with thermal oxide on silicon, followed by lithography and oxide etching with buffered hydrofluoric acid. Figure 1b (inset) presents scanning electron micrographs of devices with 12° and 27° wedge angles. Empirically, this angle can be controlled by adjustment of the photoresist adhesion using commercially available adhesion promoters. The oxide disk structures function as an etch mask for an isotropic dry etch of the silicon using XeF_2. During this dry etch, the silicon undercut is set to reduce coupling of the optical mode to the silicon support pillar. This value is typically set to ∼100 μm for 1-mm-diameter structures and over 150 μm for 7.5-mm-diameter disks; however, smaller undercuts are possible while still preserving UHQ performance. Further information on processing is provided in the Methods.

To measure the intrinsic Q-factor, devices were coupled to SMF-28 optical fibre using a fibre taper[16,17], and spectral lineshape data were obtained by tuning an external cavity semiconductor laser across the resonance while monitoring transmission on an oscilloscope. The taper coupling could be adjusted to both overcouple and undercouple the resonator[17]. All measurements were performed in the 1,500 nm band. To accurately calibrate the laser scan in this measurement, a portion of the laser output was also monitored after transmission through a calibrated Mach–Zehnder interferometer with an FSR of 7.75 MHz. Figure 2 (inset) presents a spectral scan obtained on a device with a record Q-factor of 875 million. In these measurements, the taper coupling was applied on the upper surface of the resonator near the centre of the wedge region (Fig. 1b). Modelling shows that the fundamental mode has its largest field amplitude in this region. Moreover, this mode is expected to feature the lowest overall scattering loss resulting from the three dielectric–air interfaces as well as from the silicon support pillar. An additional test that can be performed to verify the fundamental mode is to measure the mode index by monitoring the FSR. The fundamental mode features the largest mode index and hence smallest FSR. To expedite the measurement of the Q-factor in these devices, an automated system was devised in which a broad spectral scan (exceeding a full FSR) was performed and recorded onto a fast digital oscilloscope (1 GHz). The spectrum was then analysed using a fitting algorithm to identify and fit the resonator modes. This made a rapid acquisition (and identification) of the highest Q

T. J. Watson Laboratory of Applied Physics, California Institute of Technology, Pasadena, California 91125, USA; †These authors contributed equally to this work. *e-mail: vahala@caltech.edu

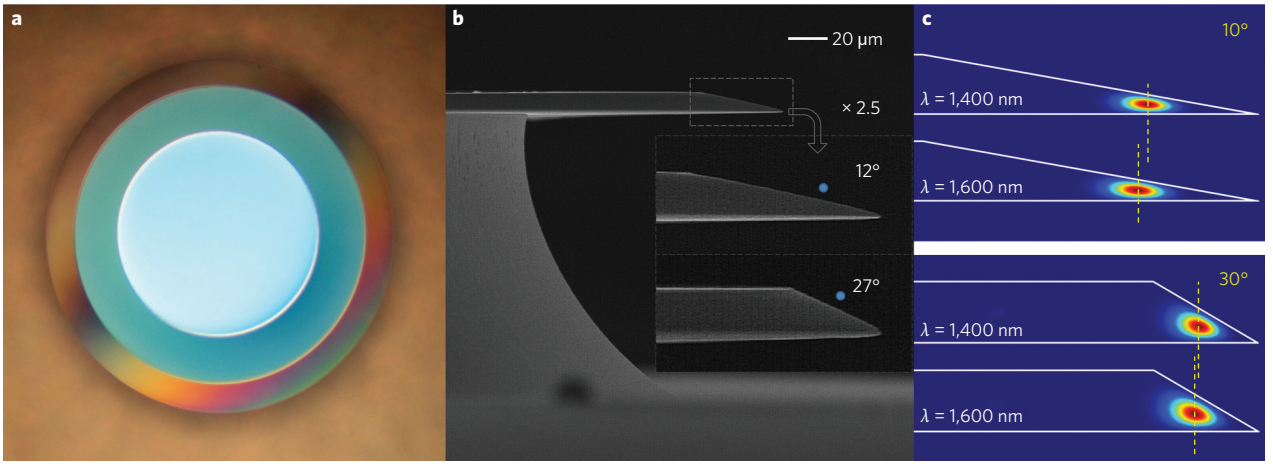

Figure 1 | Micrographs and mode renderings of the wedge-resonator from top and side views. a, Optical micrograph showing a top view of a 1-mm-diameter wedge-resonator. **b**, Scanning electron micrograph showing the side view of a resonator. Insets: slightly magnified micrographs of resonators with wedge angles of 12° (upper inset) and 27° (lower inset). Blue circles indicate the approximate locations of the taper during measurements. **c**, Calculated fundamental-mode intensity profiles in resonators with 10° and 30° wedge angles at two wavelengths. As a guide, the centre-of-motion of the mode is provided to illustrate how the wedge profile introduces a normal dispersion that is larger for smaller wedge angles.

mode possible. Spectra were taken in the undercoupled regime to obtain *Q*-values closer to the intrinsic (unloaded) value. Finite-element analysis showed that the modes can be approximately resolved into transverse electric (TE) and transverse magnetic (TM) cases, where the transverse field is parallel to the flat (lower) oxide surface. TM waves extend further into the air and have slightly lower *Q*-factors. All measurements reported are for TE waves.

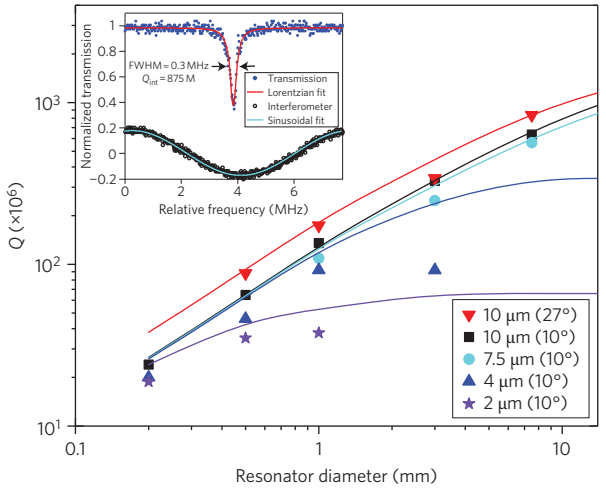

Figure 2 | Data showing measured *Q*-factor plotted versus resonator diameter with oxide thickness as a parameter. Multiple devices were measured for each data point; however, the dispersion in *Q*-values was typically low, so error bars are not shown and only the average *Q*-value device is shown. For example, the average *Q* data (red points) are taken from the following set, where each *Q*-value represents a distinct device (M, million): $D \approx 7.5$ mm, $Q \approx 799$M, 875M; $D \approx 3$ mm, $Q \approx 326$M, 331M, 367M; $D \approx 1$ mm, $Q \approx 169$M, 174M; $D \approx 0.5$ mm, $Q \approx 88$M, 91M. Solid lines show the *Q*-factor predicted by a model that accounts for surface-roughness-induced scattering loss and also material loss (fitting gives a material *Q* of 2.5 billion). The r.m.s. roughness is measured using an atomic force microscope (see Methods for values). Red data points correspond to a wedge angle of 27°. All other data are obtained using a wedge angle of ~10°. Inset: spectral scan for the case of a record *Q*-factor of 875 million. In this spectrum, the resonator is undercoupled so that the linewidth is close to the intrinsic value. However, both critical coupling and strong overcoupling are also possible by adjusting the air gap between the taper and the resonator. The sinusoidal curve accompanying the spectrum is a calibration scan performed using a fibre interferometer.

The typical coupled power in all measurements was maintained at ~1 μW to minimize thermal effects. However, there was little or no evidence of thermal effects in the optical spectrum (up to coupled power levels as high as 1 mW). Typically, these appear as an asymmetry in the lineshape and also a scan-direction-dependent (to higher or lower frequency) spectral linewidth. As a further check that thermal effects were negligible, ring-down measurements[18] were also performed on a range of devices for comparison with the spectral-based *Q* measurement. For these, the laser was tuned into resonance with the cavity and a lithium niobate modulator was used to abruptly switch off the input. The output cavity decay rate was then monitored to ascertain the cavity lifetime. Ring-down data and spectral linewidths were consistently in good agreement. This insensitivity to thermal effects is a result of the larger mode volumes of these devices in comparison to the microtoroids used in earlier work (for which thermal effects must be carefully monitored). The mode volumes in the present devices are typically 100–1,000 times larger.

Measurements showing the effects of oxide thickness and device diameter on *Q*-factor are presented in Fig. 2. Four oxide thicknesses are shown (2, 4, 7.5 and 10 μm) over diameters ranging from 0.2 mm to 7.5 mm. All data points, with the exception of the red points, correspond to a wedge angle of ~10°. The uppermost (highest *Q* at a given diameter) data correspond to a wedge angle of 27°. It is interesting to note that there was a high level of consistency in the *Q*-values measured on devices from a single chip. A complete data set for the red curve in Fig. 2 is provided in the caption to Fig. 2 to indicate the low dispersion in the *Q* data. The solid curves are a model of optical loss caused by surface scattering on the upper, wedge, and lower oxide–air interfaces and by bulk-oxide loss. In the model, surface roughness was measured independently on each of these surfaces using an atomic force microscope (AFM) (r.m.s. roughness values and additional information on the model are given in the Methods). Data corresponding to the 10° wedge angle show that *Q* increases for thicker oxides and also larger diameters. Using the model, this trend can be understood to result from loss caused primarily by scattering at the oxide–air interfaces. Specifically, both thicker oxides and larger-diameter

structures feature a reduced field amplitude at the dielectric–air interface, leading to reduced scattered power. An overall boost to the Q-factor is possible by increasing the wedge angle. In this case, the mode experiences reduced upper and lower surface scattering compared to the smaller angle case. As noted before, this behaviour contrasts with earlier work in which the wedge was used to isolate the mode from edge roughness[15]. Specifically, the larger angle case in Fig. 1b leads to higher Q-values, and a record Q-factor of 875 million for any chip-based resonator is obtained under these conditions. In general, there is reasonably good agreement between the model and the data, except in the case of the thinner oxides. For these thinner structures, there is a tendency for stress-induced buckling to occur at larger radii. This is believed to create the discrepancy with the model. The trend of improving Q with increasing wedge angle that is apparent in Fig. 2 is also confirmed by the model (Supplementary Section I).

The ability to lithographically define UHQ resonators rather than rely on the reflow process enables a multi-order-of-magnitude improvement in the control of resonator diameter and FSR. This feature is especially important in microcombs and certain nonlinear sources[12,13]. As a preliminary test of the practical limits of FSR control, two studies were conducted. In the first, a series of resonator diameters were set in a CAD file that was to be used to create a photomask. A plot of the measured FSR (fundamental mode) versus CAD file target diameter is provided in Fig. 3. The variance from ideal linear behaviour measured on five devices from different locations on the same four-inch wafer is 2.4 MHz, giving a relative variance of better than 1:4,500 (FSR ≈ 11 GHz). The inset to Fig. 3 shows that for a second set of four devices from different locations on a separate wafer, but having the same target diameter, the variance is further improved to a value of 0.45 MHz or 1:20,000. More data runs will be accumulated over time to provide better statistics, but these preliminary findings are nonetheless very encouraging. There is an overall size reduction that occurs between the mask and final etch diameter of ~10 μm (10 μm oxide). However, the above data suggest that this size reduction can be accurately calibrated.

As an application of the combination of size control and ultrahigh Q-value available using these new resonators, we then demonstrated SBLs. Although Brillouin scattering is well known in optical fibre communication, including its use for gain in narrow-linewidth fibre lasers[19], generation of slow light[20,21] and information storage[22], the realization of microcavity-based SBLs is very challenging because of the requirement to precisely match the Brillouin shift to a pair of cavity modes. Specifically, the narrow linewidth of the Brillouin gain requires better than 1:1,000 control of the resonator diameter to obtain a match, and more realistically it requires 1:10,000 control for consistent low threshold turn-on power.

To test the resonators as SBLs, pump power was coupled into the resonator through the fibre taper coupler. SBL emission was coupled into the opposing direction and routed via a circulator into a photodiode and optical spectrum analyser to monitor both the laser output power and the spectrum. The transmitted pump wave was monitored using a balanced homodyne receiver so as to implement a Hänsch–Couillaud locking of the pump to the resonator[23,24]. The threshold for SBL action is given by the expression

$$P_{\mathrm{th}} = \frac{\pi^2 n^2 V_{\mathrm{eff}}}{g_{\mathrm{b}} Q_{\mathrm{p}} Q_{\mathrm{b}} \lambda_{\mathrm{p}} \lambda_{\mathrm{b}}}$$

where n is the refractive index, V_{eff} is the mode volume, λ_{p} (λ_{b}) is the pump (lasting) wavelength, and Q_{p} (Q_{b}) is the loaded Q-factor of the pump (lasting) mode. Beyond the importance of the high cavity Q-factor evident in this expression, it is essential to maintain a large

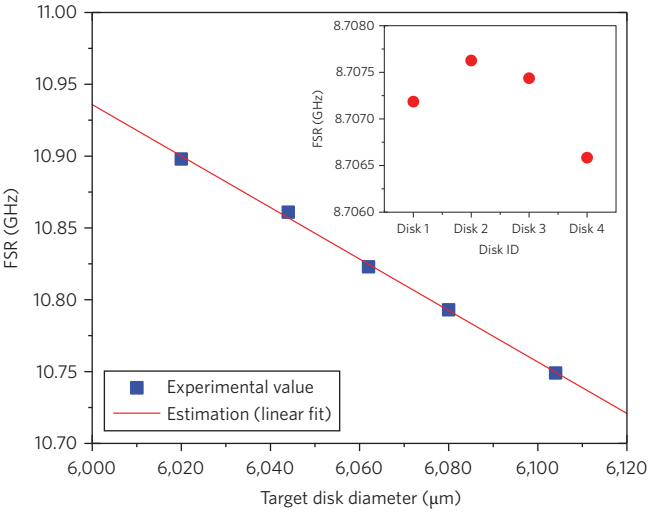

Figure 3 | Plot of measured FSR versus target design-value resonator diameter on a lithographic mask. The plot shows one device at each size for five different sizes. The r.m.s. variance is 2.4 MHz (relative variance of less than 1:4,500). Inset: FSR data measured on four devices with the same target FSR. An improved variance of 0.45 MHz is obtained (a relative variance of 1:20,000).

SBL gain parameter, $g_{\mathrm{b}}(\Delta\omega - \Omega_{\mathrm{B}})$ (where gain $= g_{\mathrm{b}} P_{\mathrm{pump}}$, $\Delta\omega$ is the FSR and Ω_{B} is the Brillouin shift). Because the gain spectrum is relatively narrow (typical full-width at half-maximum of 20–60 MHz; refs 19,25), this requires a precise match of the FSR to the Brillouin shift. Ω_{B} depends on the pump wavelength λ_{p} and phonon velocity V_{a} through the relation $\Omega_{\mathrm{B}}/2\pi = 2nV_{\mathrm{a}}\lambda_{\mathrm{p}}$. An illustration of the control possible using the new resonator geometry is provided in Fig. 4a, in which four devices with diameters of 6,020, 6,044, 6,062 and 6,080 μm (lithography mask size) were tested at a series of pump wavelengths in the 1,500 nm band. In each device, the pump wavelength was sequentially tuned along resonances belonging to the same azimuthal mode family. The minimum threshold for each device corresponds to excitation at the Brillouin gain maximum (that is, $g_{\mathrm{b}}(\Delta\omega - \Omega_{\mathrm{B}} = 0)$). The rise in threshold away from the minimum (for a given resonator diameter) reflects tuning of the Brillouin shift frequency with pump wavelength as noted above. A typical spectrum showing the emitted laser line and the pump are given in Fig. 4c. As an indication of the consistency in size and Q that is possible, all devices tested lased with minimum threshold values below 200 μW. Moreover, because of the narrow Brillouin gain bandwidth, the side mode suppression at 1 mW output power was in excess of 60 dB (measured by mixing the pump and laser waves on a photodetector and monitoring the electrical power in the beat note). The coherence properties of these Brillouin lasers are excellent and are studied in Supplementary Section II (for example, they feature subhertz Schawlow–Townes linewidths).

The Q-factor for these new resonators is not only higher in an absolute sense than what has been possible with microtoroids, but it also accesses an important regime of resonator FSR that has not been possible using microtoroids. To date, the smallest FSR achieved with the toroid reflow process is 86 GHz ($D = 750$ μm) and the corresponding Q factor is 20 million[26]. The present structures achieve their best Q-factors for FSRs that are complementary to microtoroids (FSRs less than 100 GHz). As well as the application to SBLs described, this range has become increasingly important in applications such as microcombs where self-referencing is important. Specifically, low turn-on power and microwave-rate repetition are conflicting requirements in these devices because of the inverse

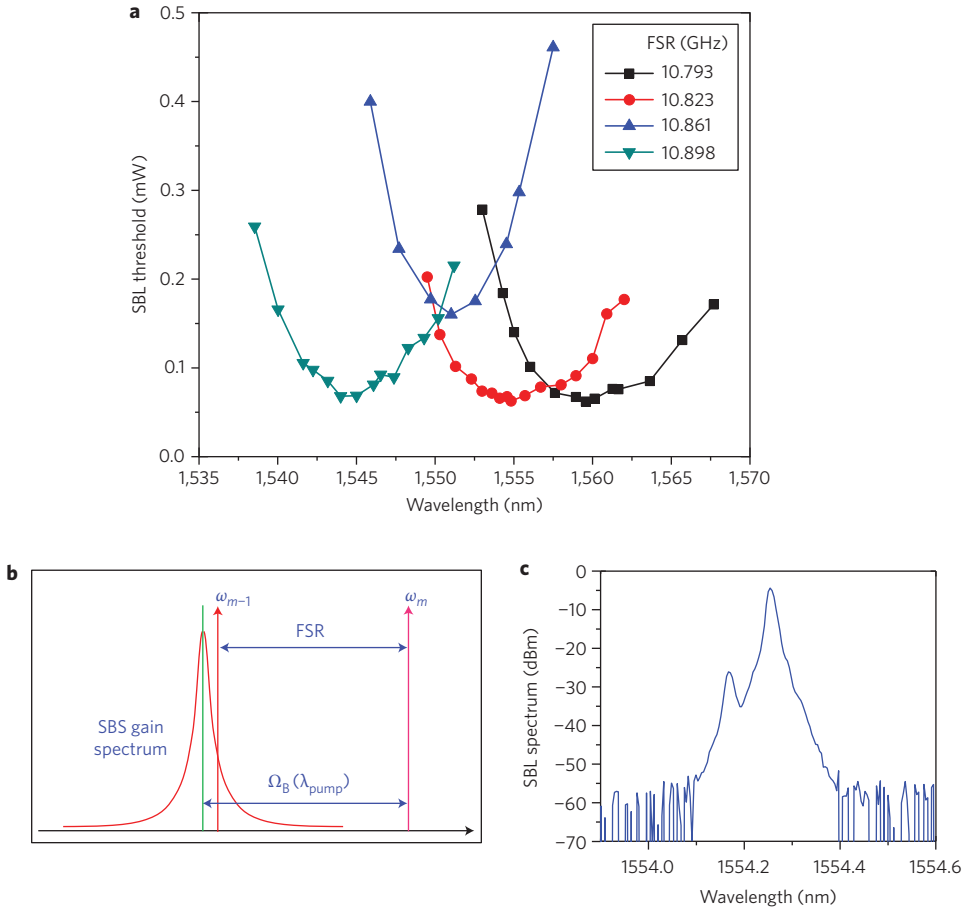

Figure 4 | Illustration of tuning control of the SBL devices. a, SBL threshold is measured as a function of pump wavelength using four slightly different resonator diameters. **b**, Illustration of control of stimulated Brillouin gain with a change in FSR and pump wavelength. **c**, Spectrum of Brillouin laser output, showing pump laser (lower peak) and laser output (higher peak). The pump wave appears weaker because the laser emission occurs along the opposite direction to the pump wave.

dependence of threshold power on FSR. However, such increases can be compensated using ultrahigh Q-values because turn-on power depends inverse-quadratically on Q (ref. 27).

The wedge angle can be shown to provide control over the zero dispersion point in spectral regions where silica exhibits anomalous dispersion. Specifically, beyond 1.3 μm, silica features anomalous dispersion; however, the wedge structure introduces a geometrical component of dispersion that is normal (Fig. 1c). Calculations show that the overall zero dispersion falls within the 1.5 μm band for the structures tested here. UHQ performance in large-area resonators is also important in rotation sensing[28] and for on-chip frequency references[29,30]. In the former case, the larger resonator area enhances the Sagnac effect. In the latter, the larger mode volume lowers the impact of thermal fluctuations on the frequency noise of the resonator[31]. There may also be potential applications of these structures to cavity optomechanics[2,3], where the ability to define the whispering gallery and a mechanical support in one lithographic step could provide an improved method to both boost optical Q while controlling mechanical eigenmodes and their damping. For example, spoke structures have been implemented in toroids to minimize clamping losses[32]. By applying the methods described here, structures like these could be implemented in the same step used to define the whispering gallery.

Although not demonstrated here, there are several ways to incorporate waveguides into these devices. For example, wafer bonding has recently been used to apply a thermal oxide structure to a second wafer containing a nitride resonator with Q-factors in

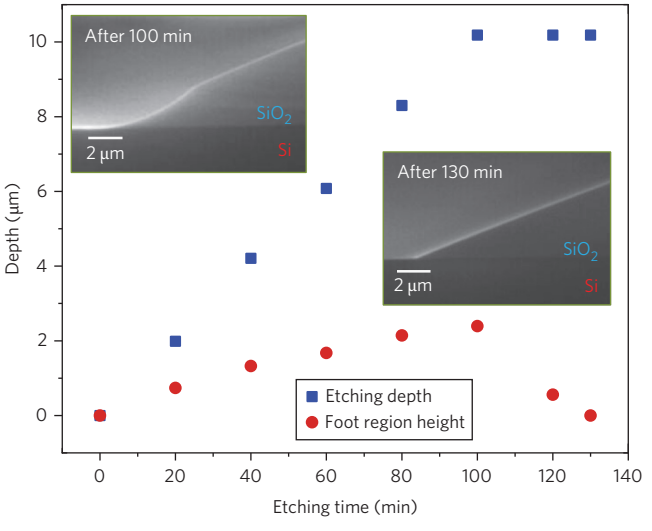

Figure 5 | Data plot showing effect of etch time on appearance of the 'foot' region in etching of a 10-μm-thick silica layer. The foot region is a separate etch front produced by a wet etch of silica and is observed empirically to adversely affect the optical Q-factor. The data show that by control of the etch time the 'foot' region can be eliminated. The upper-left inset is an image of the foot region and the lower right inset shows the foot region eliminated by an increase of the wet etch time.

the range of 20 million[33]. We are studying an adaptation of this approach to create a nitride-waveguide-coupled UHQ resonator. Such a device does not currently exist and would have a major impact on the many applications of UHQ devices. Key to this approach would be achieving precise resonator size control, which would make it possible for lithographically defined fiducial locators to register mating parts. Finally, it is important to note that an upper bound to the material loss of thermal silica has been established in this work. The value of 2.5 billion for material Q bodes well for further application of thermal silica to photonic devices. Also, while the ability to leverage thermal silica on silicon in this way is important, the techniques reported here could equally well be applied to high-quality silica deposited onto other substrates.

Methods

Disks were fabricated on (100) prime-grade float-zone silicon wafers. Photoresist was patterned using a GCA 6300 stepper on thermally grown oxide with a thickness in the range 2–10 μm. A post-exposure bake was then used to cure the surface roughness of the photoresist pattern, which acted as an etch mask during immersion in buffered hydrofluoric solution (Transene, buffer-HF improved). Careful examination of the wet etch revealed that the vertex formed by the lower oxide surface and upper surface contained an etch front distinct from that associated with the upper surface (see 'foot' region in Fig. 5, left inset). This region has a roughness level that is higher than any other surface and is a significant contributor to Q degradation. By extending the etch time beyond what is necessary to reach the silicon substrate, this foot region can be eliminated, as shown in Fig. 5 (main panel). With elimination of the foot etch front, the isotropic and uniform etching characteristic of buffered hydrofluoric solution results in oxide disks and waveguides with very smooth wedge-profiles, which enhance the Q-factors. Additionally, the oxide used in these studies was prepared in such a way as to reduce optical loss. Although the oxide layers were prepared using wet oxidation, it was found that a final dry oxidation step (24 h) at 1,000 °C was required to reliably achieve the highest Q factors. This additional step is believed to drive down the water content in the silica oxide. After a conventional cleaning process to remove photoresist and organics, silicon was isotropically etched by xenon difluoride to create an air-cladding whispering-gallery resonator. An atomic force microscope was used to measure the surface roughness of the three silica–air dielectric surfaces. For the lower surface, the resonators were detached by first etching the silicon pillar to a few micrometres in diameter and then removing the resonator using tape. The r.m.s. roughness values on 10° wedge-angle devices were 0.15 nm (upper), 0.46 nm (wedge) and 0.70 nm (lower); for the 27° wedge-angle devices these values were 0.15 nm (upper), 0.75 nm (wedge) and 0.70 nm (lower). The morphology of the lower surface is complex and the roughness is an estimate. The correlation length is on the order of a few hundred nanometres. The difference in the wedge surface roughness obtained for the large and small wedge angle cases is not presently understood.

By conducting Q versus resonator diameter studies, we conclude that scattering losses are the dominant source of loss in these resonators (Fig. 2). To estimate these losses, we adapted a general approach reported elsewhere[34–36].

Received 30 November 2011; accepted 13 April 2012; published online 20 May 2012

References

1. Vahala, K. J. Optical microcavities. *Nature* **424,** 839–846 (2003).
2. Kippenberg, T. J. & Vahala, K. J. Cavity optomechanics: back-action at the mesoscale. *Science* **321,** 1172–1176 (2008).
3. Kippenberg, T. J. & Vahala, K. J. Cavity opto-mechanics. *Opt. Express* **15,** 17172–17205 (2007).
4. Matsko, A. B. & Ilchenko, V. S. Optical resonators with whispering-gallery modes-part I: basics. *IEEE J. Sel. Top. Quant. Electron.* **12,** 3–14 (2006).
5. Ilchenko, V. S. & Matsko, A. B. Optical resonators with whispering-gallery modes-part II: applications. *IEEE J. Sel. Top. Quant. Electron.* **12,** 15–32 (2006).
6. Kippenberg, T. J., Holzwarth, R. & Diddams, S. A. Microresonator-based optical frequency combs. *Science* **332,** 555–559 (2011).
7. Aoki, T. *et al.* Observation of strong coupling between one atom and a monolithic microresonator. *Nature* **442,** 671–674 (2006).
8. Armani, D. K., Kippenberg, T. J., Spillane, S. M. & Vahala, K. J. Ultra-high-Q toroid microcavity on a chip. *Nature* **421,** 925–929 (2003).
9. Grudinin, I. S., Matsko, A. B. & Maleki, L. On the fundamental limits of Q factor of crystalline dielectric resonators. *Opt. Express* **15,** 3390–3395 (2007).
10. Grudinin, I. S., Ilchenko, V. S. & Maleki, L. Ultrahigh optical Q factors of crystalline resonators in the linear regime. *Phys. Rev. A* **74,** 063806 (2006).
11. Savchenkov, A. A., Matsko, A. B., Ilchenko, V. S. & Maleki, L. Optical resonators with ten million finesse. *Opt. Express* **15,** 6768–6773 (2007).
12. Tomes, M. & Carmon, T. Photonic micro-electromechanical systems vibrating at X-band (11-GHz) rates. *Phys. Rev. Lett.* **102,** 113601 (2009).
13. Grudinin, I. S., Yu, N. & Maleki, L. Brillouin lasing with a CaF_2 whispering gallery mode resonator. *Phys. Rev. Lett.* **102,** 043902 (2009).
14. Pant, R. *et al.* Cavity enhanced stimulated Brillouin scattering in an optical chip for multiorder Stokes generation. *Opt. Lett.* **36,** 3687–3689 (2011).
15. Kippenberg, T. J., Kalkman, J., Polman, A. & Vahala, K. J. Demonstration of an erbium-doped microdisk laser on a silicon chip. *Phys. Rev. A* **74,** 051802 (2006).
16. Cai, M., Painter, O. J. & Vahala, K. J. Observation of critical coupling in a fiber taper to silica-microsphere whispering gallery mode system. *Phys. Rev. Lett.* **74,** 051802 (2006).
17. Spillane, S. M., Kippenberg, T. J., Painter, O. J. & Vahala, K. J. Ideality in a fiber-taper-coupled microresonator system for application to cavity quantum electrodynamics. *Phys. Rev. Lett.* **91,** 043902 (2003).
18. Vernooy, D. W., Ilchenko, V. S., Mabuchi, H., Streed, E. W. & Kimble, H. J. High-Q measurements of fused-silica microspheres in the near infrared. *Opt. Lett.* **23,** 247–249 (1998).
19. Smith, S. P., Zarinetchi, F. & Ezekiel, S. Narrow-linewidth stimulated Brillouin fiber laser and applications. *Opt. Lett.* **16,** 393–395 (1991).
20. Okawachi, Y. *et al.* Tunable all-optical delays via Brillouin slow light in an optical fiber. *Phys. Rev. Lett.* **94,** 153902 (2005).
21. Zhu, Z., Dawes, A., Gauthier, D., Zhang, L. & Willner, A. Broadband SBS slow light in an optical fiber. *J. Lightwave Technol.* **25,** 201–206 (2007).
22. Zhu, Z., Gauthier, D. & Boyd, R. Stored light in an optical fiber via stimulated Brillouin scattering. *Science* **318,** 1748–1750 (2007).
23. Hänsch, T. & Couillaud, B. Laser frequency stabilization by polarization spectroscopy of a reflecting reference cavity. *Opt. Commun.* **35,** 441–444 (1980).
24. Schliesser, A., Riviere, R., Anetsberger, G., Arcizet, O. & Kippenberg, T. J. Resolved-sideband cooling of a micromechanical oscillator. *Nature Phys.* **4,** 415–419 (2008).
25. Tkach, R. W., Chraplyvy, A. R. & Derosier, R. M. Spontaneous Brillouin scattering for single-mode optical-fibre characterisation. *Electron. Lett.* **22,** 1011–1013 (1986).
26. Del'Haye, P., Arcizet, O., Schliesser, A., Holzwarth, R. & Kippenberg, T. J. Full stabilization of a microresonator frequency comb. *Phys. Rev. Lett.* **101,** 053903 (2008).
27. Kippenberg, T. J., Spillane, S. M. & Vahala, K. J. Kerr-nonlinearity optical parametric oscillation in an ultrahigh-Q toroid microcavity. *Phys. Rev. Lett.* **93,** 083904 (2004).
28. Ciminelli, C., Dell'Olio, F., Campanella, C. & Armenise, M. Photonic technologies for angular velocity sensing. *Adv. Opt. Photon.* **2,** 370–404 (2010).
29. Matsko, A. B., Savchenkov, A. A., Yu, N. & Maleki, L. Whispering-gallery-mode resonators as frequency references. I. Fundamental limitations. *J. Opt. Soc. Am. B* **24,** 1324–1335 (2007).
30. Savchenkov, A. A., Matsko, A. B., Ilchenko, V. S., Yu, N. & Maleki, L. Whispering-gallery-mode resonators as frequency references. II. Stabilization. *J. Opt. Soc. Am. B* **24,** 2988–2997 (2007).
31. Gorodetsky, M. L. & Grudinin, I. S. Fundamental thermal fluctuations in microspheres. *J. Opt. Soc. Am. B* **21,** 697–705 (2004).
32. Anetsberger, G., Riviére, R., Schliesser, A., Arcizet, O. & Kippenberg, T. J. Demonstration of ultra low dissipation optomechanical resonators on a chip. *Nature Photon.* **2,** 627–633 (2008).
33. Tien, M. C. *et al.* Ultra-high quality factor planar Si_3N_4 ring resonators on Si substrates. *Opt. Express* **19,** 13551–13556 (2011).
34. Ciminelli, C., Passaro, V., Dell'Olio, F. & Armenise, M. Three-dimensional modelling of scattering loss in InGaAsP/InP and silica-on-silicon bent waveguides. *J. Eur. Opt. Soc. Rapid Publ.* **4,** 1–6 (2009).
35. Barwicz, T. & Haus, H. Three-dimensional analysis of scattering losses due to sidewall roughness in microphotonic waveguides. *J. Lightwave Technol.* **23,** 2719–2732 (2005).
36. Payne, F. & Lacey, J. A theoretical analysis of scattering loss from planar optical waveguides. *Opt. Quantum. Electron.* **26,** 977–986 (1994).

Acknowledgements

The authors acknowledge support from the Defense Advanced Research Projects Agency under the iPhoD and Orchid programmes and also the Kavli Nanoscience Institute at Caltech. H.L. acknowledges support from the Center for the Physics of Information, and S.J. thanks the Kwanjeong Educational Foundation.

Author contributions

All authors made important contributions. H.L., T.C. and J.L. performed measurements and modelling, and contributed equally to the work. H.L. performed microfabrication of devices with assistance from T.C. and K.Y. AFM measurements were performed by H.L. and S.J. The experiments were conceived, designed and planned by H.L., T.C., J.L., O.P. and K.J.V. All authors helped to write the manuscript.

Additional information

The authors declare no competing financial interests. Supplementary information accompanies this paper at www.nature.com/naturephotonics. Reprints and permission information is available online at http://www.nature.com/reprints. Correspondence and requests for materials should be addressed to K.J.V.